Solid State Ionics 382 (2022) 115959

Contents lists available at ScienceDirect

Solid State Ionics

journal homepage: www.elsevier.com/locate/ssi

Characterization of Y and Mn co-substituted $BaZrO_3$ ceramics: Material properties as a function of the substituent concentration

Maria Balaguer [a,b,*], Yoo Jung Sohn [a], Dietmar Kobertz [c], Sergey Kasatikov [d], Andrea Fantin [d,e], Michael Müller [c], Norbert H. Menzler [a], Olivier Guillon [a,f], Mariya E. Ivanova [a,**]

[a] Institute of Energy and Climate Research: Materials Synthesis and Processing (IEK-1), Forschungszentrum Jülich GmbH, 52425 Jülich, Germany
[b] Instituto de Tecnología Química, Universitat Politècnica de València – Consejo Superior de Investigaciones Científicas, Av. Los Naranjos s/n, 46022, Valencia, Spain
[c] Institute of Energy and Climate Research: Microstructure and Properties of Materials (IEK-2), Forschungszentrum Jülich GmbH, 52425 Jülich, Germany
[d] Institute of Applied Materials, Helmholtz-Zentrum Berlin für Materialien und Energie GmbH, 14109 Berlin, Germany
[e] Institute for Materials Science and Technologies, Technical University Berlin, 10623 Berlin, Germany
[f] JARA Energy, Aachen-Jülich, Germany

ARTICLE INFO

Keywords:
Ceramic mixed proton-electronic conductors
Proton conducting ceramic cells
Ceramic membranes for H_2 separation
B-side double substituted $BaZrO_3$
Mn and Y co-substituted $BaZrO_3$
$A^{(II)}B^{(IV)}O_3$ perovskites
$BaZr_{0.8}Y_{0.2-x}Mn_xO_{3-\delta}$
NEXAFS

ABSTRACT

Innovations in materials science are the key element for solving technological challenges. Various energy and environmental applications require designing materials with tailored compositions, microstructures and specific target-oriented performance. Y and Mn co-substituted $BaZrO_3$, e.g. $BaZr_{0.85}Y_{0.15}Mn_{0.05}O_{3-\delta}$, has previously attracted attention as a membrane material for H_2 separation from gas mixtures due to its mixed proton-electron conductivity leading to appreciable levels of H_2-flux at elevated temperatures and its good thermo-chemical stability under reducing environments. In the present work, we developed ceramic materials within the $BaZr_{0.8}Y_{0.2-x}Mn_xO_{3-\delta}$ series, where x = 0.02–0.15. The study of their functional properties in dependence of the Y-to-Mn ratio disclosed that thermal expansion and hydration decrease by increasing the Mn content as well as the total electrical conductivity. In addition to that, XPS analysis and near edge X-ray absorption fine structure spectra (NEXAFS) in the vicinity of O K-edge and Mn $L_{2,3}$-edges indicated that the Mn atoms oxidation state in the surface and in the bulk range from Mn^{2+} to Mn^{4+} depending on the ambient conditions that can be encountered in MPEC electrodes, which it is suggested to be related with a hydration mechanism mediated by Mn oxidation and subsequent proton attachment to oxygen neighbors, similar to LSM.

1. Introduction

Yttrium substituted $BaZrO_3$ cubic perovskite is one of the most prominent proton conductors and most studied as solid state electrolyte in a number of electrochemical devices. The addition of multivalent Mn through partial substitution on B site in the perovskite turns this oxide to a mixed proton-electronic conductor of the type $BaZr_{0.8}Y_{0.2-x}Mn_xO_{3-\delta}$ where x = 0.02–0.15 (BZYMX). The simultaneous contribution of triple mixed protonic-electronic-oxygen ionic conductivity allows to extend the reaction zone beyond the triple phase boundary across the bulk. Several further options for applications arise from this triple conductivity, e.g. in the design of electrode material for proton conducting ceramic fuel/electrolysis cells, or as H_2 permeable membrane in extraction/reaction devices. Indeed, thick ceramic membrane of 10 mol % Y and 5 mol% Mn co-substituted $BaZrO_3$ (BZYM5) was reported firstly by our group to exhibit H_2 permeation in the order of 10^{-3} $mL \bullet min^{-1} \bullet cm^{-2}$ (1000 °C) [1], thus demonstrating clearly the potential of adding Mn towards achieving tailored electrical properties.

From the defect chemistry point of view, Y^{3+} ions occupying Zr^{4+} sites act as acceptor dopants, Y_{Zr}', so being responsible for the oxygen vacancies formation, according to the Eq. 1 in Kröger-Vink notation [2].

* Corresponding author at: Instituto de Tecnología Química, Universitat Politècnica de València – Consejo Superior de Investigaciones Científicas, Av. Los Naranjos s/n, 46022, Valencia, Spain
** Corresponding author.
E-mail addresses: mabara@itq.upv.es (M. Balaguer), m.ivanova@fz-juelich.de (M.E. Ivanova).

https://doi.org/10.1016/j.ssi.2022.115959
Received 21 January 2022; Received in revised form 16 May 2022; Accepted 26 May 2022
Available online 8 June 2022

$$2BaCO_3 + 2(1-x)ZrO_2 + xY_2O_3 \rightarrow 2Ba_{Ba}^{X} + 2(1-x)Zr_{Zr}^{X} + 2xY_{Zr}^{'} + xV_O^{\bullet\bullet} + 6O_O^{X} + O_{2(gas)} + 2CO_{2(gas)} \quad (1)$$

The number of oxygen vacancies relates to the hydration ability of the material, i.e. to the proton concentration, which is proportional to the proton conductivity of the material. Mn^{x+} ions occupy Zr^{4+} sites as well, but their role is even more complex since they have multiple oxidation states. According to Poulsen et al. [3], Manganese species exist as Mn^{2+}, Mn^{3+} and Mn^{4+} in $(La_{1-x}Sr_x)_{(y)}MnO_{3\pm\delta}$ (LSM). Considering these three species are present also in the $BaZr_{0.8}Y_{0.2-x}Mn_xO_{3-\delta}$, Mn^{2+} and Mn^{3+} being on Zr^{4+} sites are expected to act as acceptor dopants i.e. Mn''_{Zr} and Mn'_{Zr}, similarly to Y'_{Zr}, being responsible for either oxygen vacancies or electron holes generation, while the oxidized Mn^{4+} will have neutral effect on the charge balance being Mn_{Zr}^{x}. Such transition of the Mn species from one to another oxidation state will substantially lead to electronic defects being electrons or electron holes ($h^{\bullet}$) and will add electronic contribution to the overall conduction of the material.

Keeping this complex background in mind, our effort is directed towards studying the effect of the transition metal concentration (on extent of the Y) on the fundamental material properties, e.g. phase and structural evolution, thermal behavior during sintering and microstructure, but also including hydration behavior and electrical conductivity. In this work we study a series of Y and Mn co-substituted $BaZrO_3$ having a general formula $BaZr_{0.8}Y_{0.2-x}Mn_xO_{3-\delta}$, where x = 0.02, 0.05 and 0.1, henceforth referred to as BZYM2, BZYM5 and BZYM10 (BZYMX). The levels of mixed conduction in such ceramics and also their other basic properties are significantly influenced by the interplay between the chemical composition and the environmental conditions, hence elucidating these interconnected effects is at the focus in this study.

2. Experimental

2.1. Sample preparation

2.1.1. Powders

$BaZr_{0.8}Y_{0.2-x}Mn_xO_{3-\delta}$ compounds with Mn contents ranging between 2 and 15 mol% were prepared via the solid state synthesis route (SSR) from $BaCO_3$ and the corresponding oxides (Sigma Aldrich). Starting materials were tumble mixed in stoichiometric amounts, milled with ZrO_2 milling media in ethanol for 24 h and, after drying, heat treated at 1400 °C for 6 h in air. After this step, the powders were milled for 24 h.

Samples with higher Mn loads (BZYM15 and BZM20) were synthesized also via the Pechini synthesis route in order to ascertain the solubility limits for the substituents. ($BaNO_3$, $ZrO(NO_3)$, $Y(NO_3)_3{\cdot}4H_2O$, and $Mn(NO_3)_2{\cdot}xH_2O$ (Sigma Aldrich) were mixed in a homogeneous solution. After the complete dissolution, citric acid (Sigma Aldrich) was added as chelating agent to prevent partial segregation of metal components, and ethylene glycol was added to polymerize with chelating agent and produce an organometallic polymer (in a molar ratio 1: 2: 4, respectively). The complexation was followed by dehydration at low temperature (up to 300 °C) and finally, the thermal decomposition of the precursors at 600 °C and the formation of the perovskite structural phase at 1400 °C. After calcination the powder was ball milled during 24 h to eliminate the agglomerates.

2.1.2. Sintered samples

Specimens were shaped from the synthesized homogeneous powders by means of uniaxial pressing at 30 $kN{\bullet}cm^{-2}$ for 90 s. The sintering of shaped SSR-specimens took place at 1700 °C for 10 to 30 h in ambient air and in synthetic air with heating/cooling rate of 2 $K{\bullet}min^{-1}$. Sacrificial powder was used to protect specimens from Ba loss at these harsh sintering condition. Small batches of powder were additionally heat treated at 1500 °C and 1600 °C for the quantification of Ba loss over the studied temperature range.

2.1.3. Samples for thermogravimetry

Pellets of BZYM = $BaZr_{0.8}Y_{0.2-x}Mn_xO_{3-\delta}$ (x = 0.02; 0.05; 0.1) were sintered at 1600 °C for 10 h (in air) and crushed down into smaller pieces, grinded manually and sieved to obtain fractions in the range 200–300 μm, thus avoiding water adsorption. 0.5–1.0 g of these coarse fractions were used for each measurement.

2.1.4. Samples for X-ray Photoelectron Spectroscopy (XPS) and Near-Edge X-ray Absorption Fine Structure (NEXAFS) Spectroscopy

Three groups of powder samples with single phase compositions were prepared: *i)* pristine BZYM10 (used for XPS and NEXAFS: from stoichiometric oxide/carbonate mixture via the solid state synthesis at 1600 °C/10 h in air; *ii)* reduced BZYM10: pristine powder specimen was subjected to reduction in 10 vol% H_2 in Ar mixture at 700 °C/20 h. The powder with violet-grey colour was then stored in a glove-box; *iii)* oxidized BZYM10: pristine powder was isostatically pressed, cube-shaped and subjected to air-oxidation in autoclave at temperatures 250–550 °C under p_{O2} of about 500 bar over 2 days (preparation in Max Planck Institute FKF, Stuttgart). Brown coloured specimen was then stored in a fridge. In addition to these three kinds of specimens, various highly pure $Mn^{(+II)}O$, $Mn_2^{(+III)}O_3$ and $Mn^{(+IV)}O_2$ (Sigma Aldrich) were used as reference compounds.

2.2. Characterization techniques

2.2.1. ICP-OES

Inductively coupled plasma optical emission spectrometry (ICP-OES) analysis was performed at ZEA-3 of Forschungszentrum Jülich GmbH and it was used to monitor chemical composition of the $BaZr_{0.8}Y_{0.2-x}Mn_xO_{3-\delta}$ materials by quantification of the cation content. 50 mg sample powder was mixed with 0.25 g lithium borate in a Pt/Au-crucible and then was heated at 1000 °C for 30 min. The melt was dissolved in 30 mL HCl (5%) and filled in 50 mL volumes. The samples were measured twice in 1:10 ratio of dilution and the mean result of three emission lines per element was used for quantification. Relative standard deviation is 1–3%.

2.2.2. XRD

Powder X-ray diffraction (XRD) patterns of $BaZr_{0.8}Y_{0.2-x}Mn_xO_{3-\delta}$ as prepared and sintered were recorded in the 2 theta range from 10° to 80° using D4 ENDEAVOR diffractometer by Bruker AXS with CuKα radiation (λ = 1.54 Å) and a LynxEye detector in Bragg-Brentano geometry. Phase identification was carried out with ICDD PDF2-Database (Release 2004) and X′ Pert Highscore Plus (by PANalytical). The TOPAS V4 software (Bruker AXS) was used to determine the lattice parameters and for Rietveld refinements. The stoichiometry of each phase is fixed for the Rietveld refinement and the starting crystal structure model was obtained from the Inorganic Crystal Structure Database (ICSD).

2.2.3. PSD

Particle size distribution for all powders was controlled using LA-950 V2 laser diffractometer by Horiba.

2.2.4. Dilatometry

Compacted samples for investigating the sintering behavior as a function of composition were prepared from mixed carbonate/oxide powder with three different Mn contents (2–10 mol%). The shrinkage rate was recorded as a function of the time and the temperature in the

range of 30 °C to 1600 °C in dry air with a dilatometer DIL 402C by Netzsch Company (Germany). In order to determine the coefficient of thermal expansion (CTE), specimens with dimensions 5x5x25 mm^3 and perfectly parallel square planes were prepared by bar-shaping and sintering at 1700 °C for 10 h. The CTE measurement was performed in the range of 30–1400 °C in heating and cooling regime in air using a dilatometer DIL 402C by Netzsch Company (Germany).

2.2.5. SEM

Microstructural analysis of materials from the series $BaZr_{0.8}Y_{0.2-x}Mn_xO_{3-\delta}$ were performed via a SEM (Ultra 55, Zeiss, Oberkochen, Germany) equipped with EDX (INCA, Oxford Instruments, Oxford, UK) in secondary electrons and backscattering modes.

2.2.6. Thermogravimetry

The thermogravimetric data were collected by a STA 449F1 instrument provided by Netzsch, Germany, with an adapted steam generator to produce a well-defined moisture in the measurement chamber. Annealed Al_2O_3 crucible as species container on top of a sample holder with Pt10/Rh-Pt thermocouple (type S) was implemented in a water-resistant furnace. In order to start the measurements with H_2O-free samples the powder was first heated up with a rate of 15 K/min to 900 °C in dry Ar flow introduced to the chamber and kept there until a constant weight was given.

Water uptake as a function of the partial pressure of H_2O (p_{H2O}) at constant temperature: Two sets of experiments were performed both at constant temperatures of 350 °C and 800 °C, respectively, in steps with various water content. The mass of water was determined using the mol number for water $n = m_{H2O} / M_{H2O}$, rearranged by the ideal gas law $m_{H2O} = V\ M_{H2O}\ p / (R\ T)$ to a mass flow per time $\dot{m}$ between 0 and 15 g h^{-1} and volume of the carrier gas $\dot{V}$ between 2 and 16 l h^{-1}. The carrier gas Ar was saturated with H_2O by feeding a peristaltic mass-flow of water continuously in the steam generator. With a variation of the mass flow the partial pressure of H_2O was retained and could be fixed. At each partial pressure, at least 5 repeating runs with humidified Ar up to constant weight change of the sample were performed, followed by a flow of dry Ar until the weight was back to the initial state. This procedure was continued up to 3.4 bar H_2O partial pressure ($\dot{m}$: 12.6 g h^{-1}, $\dot{V}$: 5 L h^{-1}, T: 140 °C). In order to distinguish the water uptake as a physical process from a chemical one, reversibility experiments were carried out from high to low partial pressures of H_2O. No weight change was observed between uptake and release; hence neither a chemical reaction nor decomposition could be supposed. The TG curves were corrected for buoyancy by measuring the weight of an empty crucible over the temperature range without and with humidification ($p_{H2O} = 1$ bar).

Water uptake as a function of the temperature at constant p_{H2O}: The powder was first heated up to 900 °C in dry Ar flow, heating rate was 15 K•min^{-1}. After 1 h at 900 °C, the gas was switched to wet Ar (pH_2O = 42.5 mbar) and the specimen was kept for 2 h before measuring. The water uptake was measured during cooling from 900 °C to 300 °C with cooling rates: 1 K•min^{-1} for 900–600 °C, 0.6 K•min^{-1} for 600–400 °C and 0.3 K•min^{-1} for 400–300 °C. The TG curves were corrected for buoyancy.

2.2.7. Electrical measurements

The electrochemical impedance spectroscopy (EIS) was conducted in the range 200–900 °C in dry and moist 2 vol% H_2 in Ar with Alpha-A High Performance Frequency analyser (Novocontrol Technologies GmbH, Germany), equipped with ZG4 test interface and WinDeta software. Saturation of 2.5 vol% H_2O was achieved by bubbling the gas through water at room temperature. For drying the gas, a commercial molecular sieve was used as a desiccant in the ProGasMix™ (NorECs, Norway). The disc-shaped sample, initially contacted with Pt, was mounted in the ProboStat™ holder (NorECs, Norway) and contacted pairwise with 4 Pt-wires. Test-sample was heated to 900 °C (2 K•min^{-1} ramp) in the corresponding atmosphere and held for a few hours at this temperature. Frequency sweeps were recorded during the cooling cycle from 100 Hz to 10 MHz with temperature steps of 50 °C and 2 h holding times at each temperature. Stray capacitance of 5 pF, originating from the measurement rig, was subtracted from the raw data. For sake of reproducibility, measurements were repeated.

To separate grain boundary from the grain interior contribution, ZView software was used for fitting the impedance spectra to serial equivalent circuit $(R_{GI}CPE_{GI})(R_{GB}CPE_{GB})(R_ECPE_E)$ with sub-circuit consisting of resistors (R) and constant phase elements (CPE) connected in parallel, according to the brick-layer model [4]. Subscripts GI, GB and E stay for grain interior, grain boundary and electrode contributions, respectively. For ascribing physical processes to the different sub-circuits effective capacitances were calculated using the following equation (Eq. 2), [5]:

$$C = Y^{1/n} R^{\left(\left(\frac{1}{n}\right)-1\right)} \tag{2}$$

Specific conductivities were then obtained from the geometrical resistances and capacitances (corrected for the sample geometry). The grain interior conductivity, σ_{GI}, was calculated by inverting the geometrical grain interior resistance, R_{GI}, while the specific grain boundary conductivity, $\sigma_{sp.GB}$, was calculated from Eq. 3 under the assumption that the dielectric constants of grain boundaries and grain interior are approximately equal:

$$\sigma_{sp,GB} = \frac{L}{A}\left(\frac{C_{GI}}{C_{GB}}\right)\frac{1}{R_{GB}} \tag{3}$$

Activation energies for grain interior ($E_{a,GI}$) and specific grain boundary ($E_{a,sp.GB}$) conductivities were calculated using the Arrhenius equation, where A_0 is the pre-exponential factor (Eq. 4):

$$\sigma = \frac{A_0}{T} exp\left(-\frac{E_a}{RT}\right) \tag{4}$$

2.2.8. XPS

X-Ray Photoelectron Spectroscopy (XPS) of the pristine sample with largest concentration of Mn, i.e. BZYM10, was carried out at ZEA-3 of Forschungszentrum Jülich GmbH. The analysis was conducted using Phi5000 VersaProbe II instrument (ULVAC-Phi Inc., USA) with Al K-alpha source, monochromatic (1.486 keV), with X-Ray settings as follows: 50 W, 15 kV, 200 μm spot. And furthermore: for the survey 187.5 eV pass energy, 0.8 eV step, 100 ms/step were applied, while for the detail 23.5 eV pass energy, 0.1 eV step, 100 ms/step were used. Quantification was done in at. % with an error of ≤10%, normalized to 100 at. %, Shirley-background, empirical relative sensitivity factors. Charge correction was done by setting the main C 1 s peak to 285 eV.

2.2.9. NEXAFS

The NEXAFS measurements were performed at the RGL-PES station at the synchrotron light source BESSY II of Helmholtz-Zentrum Berlin. In order to obtain information on oxidation states and surrounding symmetry of Mn atoms in the studied samples, near edge X-ray absorption fine structure (NEXAFS) spectra in the vicinity of O K-edge (533 eV) and Mn $L_{2,3}$-edges (L2: 641; L3: 653 eV) were recorded. Energy scans with a step of 0.1 eV and 1 s/step were employed, for a total measurement time of about 1 h per edge. The spectra were measured at an incident photon angle of 55° with energy resolution better than $E/\Delta E = 2000$ and were subsequently normalized by the incident photon flux and the synchrotron ring current. Calibration of the photon energy scale was performed by measuring the Au 4f7/2 photoelectron line (84.0 eV) of a gold single crystal. Three main BZYM10 samples were studied: the pristine one, the oxidized one and the reduced one. In addition, reference Mn oxide powders were studied: MnO, Mn_2O_3 and MnO_2. The spectra were

recorded in two different modes: the total electron yield (TEY) mode (surface sensitive: ~10 nm) and the fluorescence yield (FY) mode (bulk-sensitive: ~100 nm). For the TEY mode a Keithley ammeter was used to record the drain current and for the FY mode a BRUKER detector was utilized. Prior to the measurements, all the samples were placed on a conductive duct tape in oxygen-free atmosphere. Note that the reduced specimen was prepared and directly transferred from a glovebox (Ar atmosphere) to the experimental station (ultra-high vacuum) without any oxygen exposure in order to best preserve its reduced state.

2.2.10. *Thermo-chemical stability in simulated WGSR operation conditions*

Powder specimens of finally sintered single phase BZYM5 material were placed on an Al_2O_3 holder in a tubular oven and subjected to two types of gas compositions, simulating the feed gas, i.e. syngas with addition of steam, and retentate in a water gas shift membrane reactor (WGSMR). Schematic of the used experimental setup and further details can be found in our previous works [6,7]. The *Syngas* consisted of 34 vol % CO; 51 vol% H_2O; 15 vol% H_2, while the *Retentate* consisted of 90 vol % CO_2; 9.9 vol% H_2O; 0.1 vol% H_2, in correspondence to the usual design of such a reactor in coal gasification process. The samples were exposed for 72 h at 600 °C to 900 °C with temperature step of 100 °C. The phase composition of the exposed powder specimens was subsequently investigated by means of XRD analysis.

2.2.11. *Thermo-chemical compatibility with other ceramic materials*

i) BZYM10 ceramic powder (sintered at 1600 °C/10 h and wet ball milled) was mixed with terpineol and ethylcellulose (5 wt%) to obtain a paste, which was then brush painted on top of a polished pellet made of $BaZr_{0.7}Ce_{0.2}Y_{0.1}O_{3-\delta}$ (BZCY721) proton conductor (sintered at 1600 °C/10 h). After drying the top BZYM10 layer, heat treatment took place at 1080 °C for 3 h. Polished cross-section of the coated pellet was then microscopically inspected (SEM); *ii)* BZYM10 ceramic powder (sintered at 1600 °C/10 h) was wet (ethanol) ball mixed for a few hours with $La_{0.8}Sr_{0.2}MnO_{3-\delta}$ (LSM) powder in 1:1 mass ratio. This ratio was selected to simulate the chemical composition of a candidate cer-cer composite. After drying, heat treatment took place at 1080 °C for 3 h and the resulted powder was analyzed by means of XRD.

3. Results and discussion

3.1. *Ba stoichiometry*

BZYMX specimens with variation of Y/Mn ratio were produced from stoichiometric mixtures of Ba carbonate and the corresponding oxides via the conventional solid state reaction, and subsequently sintered. It is well known that during the heat treatment at temperatures above 1300 °C, certain amount of Ba contained in the $BaZrO_3$-based ceramics evaporates. Such ceramics exhibit disadvantages in terms of their functional properties caused by the loss of Barium. As it was previously reported [8], Barium vacancies formation is thermodynamically less favorable than the formation of Yttrium donor defects. Their concentration will naturally depend on the Ba loss magnitude, meaning that more Yttrium ions will occupy the A sites. As a consequence, less Yttrium ions will act as effective acceptor dopants occupying B sites in the BZYMX perovskites. The overall effect on the material properties will be negative with less hydration sites and reduced proton conductivity expected. Therefore, strategies to compensate Ba loss are needed and they may include *i)* implementation of novel sintering methods leading to sufficient densification at temperatures lower than the conventional ones (above 1600 °C); *ii)* over-stoichiometric synthesis approach; *iii)* sacrificial Ba-rich powder over the samples to be sintered; *iv)* sacrificial Ba-rich powder positioned in the vicinity to the samples to be sintered in a covered crucible [9]; *v)* sintering in CO_2 free atmosphere (e.g. synthetic air).

Working with the over-stoichiometric approach as in the present case requires a precise Ba loss quantification. For this purpose, BZYM5 specimens were subjected to heat treatment at four temperatures from 1400 °C to 1700 °C/30 h in air and their chemical compositions were verified by means of ICP-OES. In the investigated temperature range, Ba loss was estimated to be around 2.5 to 3.5 mol%, Fig. 1a. Adding about 3–3.5 mol% Ba above the nominally required stoichiometry led to BZYMX specimens with precise actual Ba stoichiometry after sintering at 1700 °C for 30 h as it can be inferred from Fig. 1b.

3.2. *Phase and structural analysis*

Phase and structural characteristics of BZYMX compositions with variation in Mn content after solid state synthesis at 1400 °C (powders) and sintering at 1700 °C (pellets), as well as after Pechini synthesis at 1400 °C for BZYM15 and BZM20 were investigated by means of XRD analysis. Results are depicted in Fig. 2 and Fig. 3, respectively. As it can be observed from the figures (and also from Fig. S1 in the *Supporting Information* section), in both thermal treatment conditions the single cubic phase of Pm-3 m symmetry is retained in compounds with up to 10 mol% Mn substitution additionally to the Y on Zr sites. Above this concentration, there are multiple secondary phases formed besides the main perovskite one. This can be observed for BZYM15 and BZM20 specimens synthesized both via the solid state synthesis (Fig. 2) and the

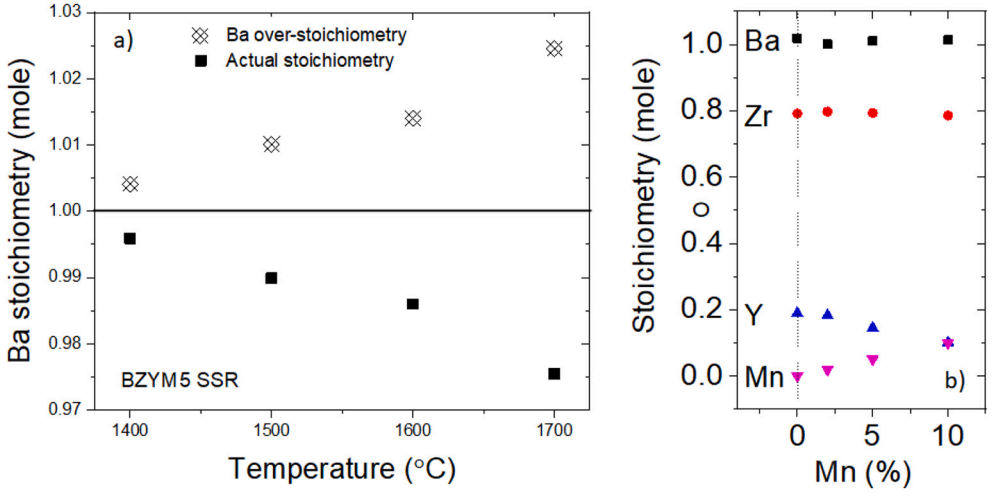

Fig. 1. a) Actual Ba stoichiometry of materials form the series $BaZr_{0.8}Y_{0.2-x}Mn_xO_{3-\delta}$ verified by ICP-OES analysis. The recommended over-stoichiometry is indicated with non-bulk symbols; b) Chemical composition of $BaZr_{0.8}Y_{0.2-x}Mn_xO_{3-\delta}$ with Ba over-stoichiometry, verified by means of ICP-OES after sintering at 1700 °C for 30 h.

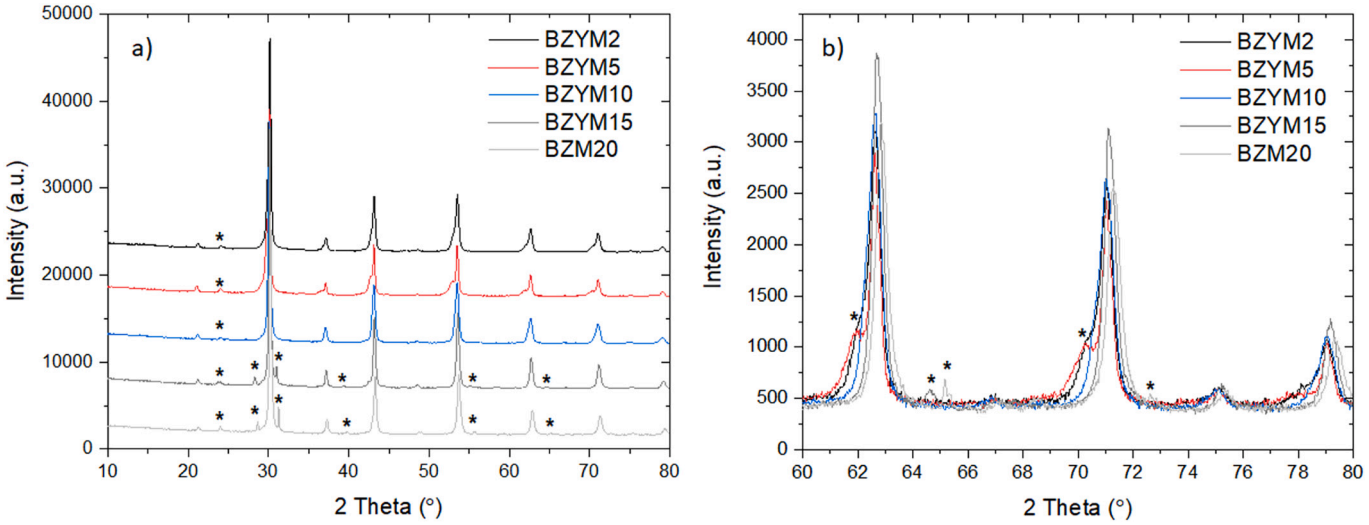

Fig. 2. XRD patterns of a) powder specimens of the series $BaZr_{0.8}Y_{0.2-x}Mn_xO_{3-\delta}$ where x = 0.02; 0.05; 0.1; 0.15 and 0.20 (BZYM2, BZYM5, BZYM10, BZYM15, BZM20 respectively) after conventional solid state synthesis at 1400 °C for 6 h; b) Magnified XRD spectra excerpt in the 2θ range of 60–80°. Secondary phases are marked with an asterisk.

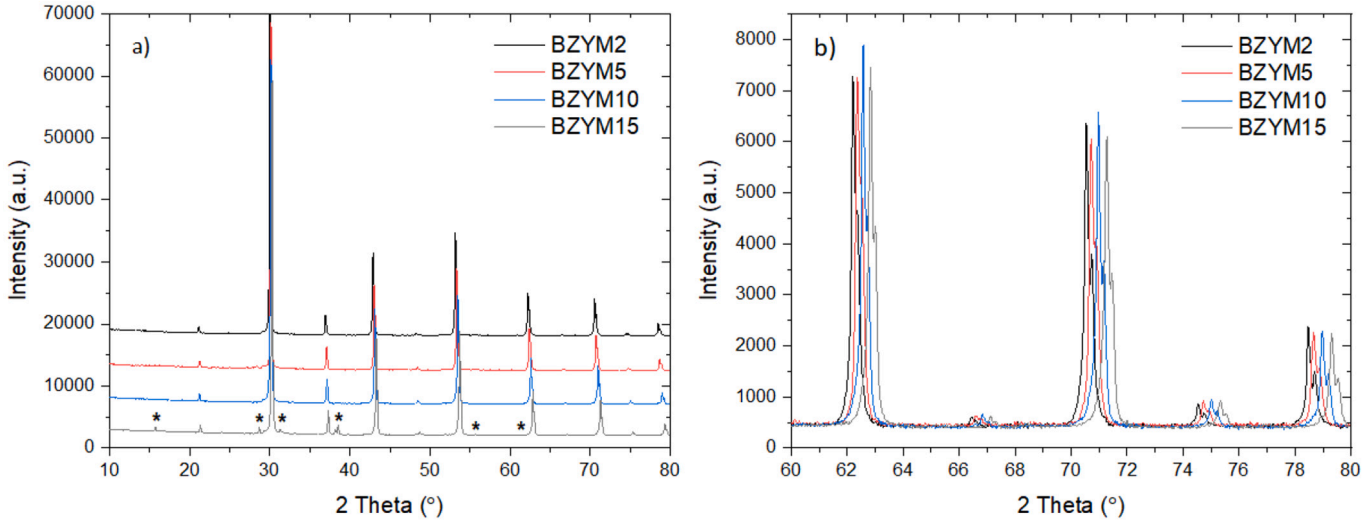

Fig. 3. XRD patterns of a) polished specimens of the series $BaZr_{0.8}Y_{0.2-x}Mn_xO_{3-\delta}$ where x = 0.02; 0.05; 0.1 and 0.15 (BZYM2, BZYM5, BZYM10 and BZYM15, respectively) sintered at 1700 °C for 10 h; b) Magnified XRD spectra excerpt in the 2θ range of 60–80°: peaks shift to the higher 2θ values with increasing the Mn content. Secondary phases are marked with an asterisk.

Pechini route (Fig. S2, section *Supporting Information*). There is a shift of Bragg reflections to the higher 2θ values with decreasing the Y/Mn ratio, as illustrated in Fig. 3b, which is observed specifically for specimen treated at the higher temperature. The reason for this is the crystal lattice shrinkage with adding more Mn (ionic radius r_i of Mn ($r_{i,Mn3+}$ = 0.58 Å; $r_{i,Mn4+}$ = 0.53 Å) is smaller than that of Y ($r_{i,Y3+}$ = 0.9 Å) and Zr ($r_{i,Zr4+}$ = 0.72 Å)). This effect is more pronounced at the sintering temperature of 1700 °C, while there is almost no shift for the BZYM2–10 at T = 1400 °C. In fact, the incorporation of substituents in the host lattice is more complete at higher temperatures.

Table 1 summarizes data about phase composition and key structural parameters (lattice parameter, crystallite size, theoretical density) of the single phase BZYMX compounds determined by means of XRD analysis at RT, after SSR and sintering. Similar structural data collected for Pechini-synthesized specimens can be found in Table S1, section *Supporting Information*. Fig. 4 illustrates the change of lattice parameter *a* (in black) determined for BZYMX materials in comparison to several selected reference values (in blue), and finally the grain size (in red) with the Y/Mn ratio. As it can be observed from the figure, lattice parameter depicted in the figure increases linearly with increasing the Y/Mn ratio (at decreased Mn content) according to the Vegard's law. This observation is also in line with the lattice shrinkage at equal oxygen deficiency (δ = 0.1) indicated by the XRD patterns of BZYMX specimens. Furthermore, comparing the obtained lattice parameters of the Y/Mn co-substituted materials with reference values for Y-substituted $BaZrO_3$, data are in good agreement. No significant variations in the crystallite size, which keeps in the range 182–185 nm, can be also observed from the figure. The theoretical density of the BZYMX compounds is in the range 6.02–6.07 g•cm^{-3}, which is some lower than that of the pristine $BaZrO_3$ (6.20 g•cm^{-3}).

3.3. Sintering behavior

The sintering behavior of compacted mixed oxide/carbonate specimens with different Y/Mn ratio was investigated in the temperature range of 30 to 1600 °C in air by means of dilatometry. The result is

Table 1
Summary of key structural parameters for materials in the $BaZr_{0.8}Y_{0.2-x}Mn_xO_{3-\delta}$ (x = 0; 0.02; 0.05; 0.1; 0.15) series and $BaZr_{0.8}Mn_{0.2}O_{3-\delta}$ (BZM20) and $BaZr_{0.5}Mn_{0.5}O_{3-\delta}$ (BZM50) prepared via the solid state reaction at 1400 °C and sintering at 1700 °C. BZ = $BaZrO_3$; BZYM = $BaZr_{0.8}Y_{0.2-x}Mn_xO_{3-\delta}$; BZY20 = $BaZr_{0.8}Y_{0.2}O_{3-\delta}$;

Mn $_{nominal}$ (mol. %) (Specimen label)		0 (BZY20)	2 (BZYM2)	5 (BZYM5)	10 (BZYM10)	15 (BZYM15)	20 (BZM20)	50 (BZM50)
Parameter	Synthesis conditions							
Phase composition	SSR 1400 °C/6 h	BZY20 (31%) BZ (69%)	BZ (62%) BZYM (37%) $BaCO_3$ (1%)	BZ (43%) BZYM (54%) $BaCO_3$ (3%)	BZ (71%) BZYM (27%) $BaCO_3$ (2%)	BZ (92%) $Ba_4Mn_3YO_{11.5}$ (6%) $BaCO_3$ (2%)	BZ (92%) $Ba_4Mn_3YO_{11.5}$ (7%) $BaCO_3$ (1%)	BZ (44%) $Ba_4Mn_3YO_{11.5}$ (16%) $BaCO_3$ (1%) $Ba_4Mn_3O_{10}$ (33%) Ba_2ZrO_4 (4%) $BaMnO_3$ (2%)
	Sint. 1700 °C/30 h	BZ (15%) $BaZr_{0.8}Y_{0.2}O_{3-\delta}$ (85%) (*10 h)	BZYM	BZYM	BZYM	BZYM (97%) Y_2O_3 (<1%) $Ba_6Mn_5O_{16}$ (2%) (*1600 °C/10 h)	BZ (94%) $Ba_4Mn_3YO_{11.5}$ (6%) (*10 h)	–
Space group/Lattice parameter *a* (Å) (in a case of multiple phases, the main zirconate phase is considered only)	SSR 1400 °C/6 h	BZY: Pm-3 m/ 4.23(3) BZ: Pm-3 m/ 4.198(3)	BZ: Pm-3 m/ 4.198(3) BZYM: Pm-3 m/ 4.23(1)	BZ: Pm-3 m/ 4.194(3) BZYM: Pm-3 m/ 4.236(9)	BZ: Pm-3 m/ 4.195(3) BZYM: Pm-3 m/ 4.215(9)	Pm-3 m/ 4.191(2)	Pm-3 m/ 4.184(2)	Pm-3 m/ 4.184(3)
	Sint. 1700 °C/30 h	Pm-3 m/ 4.233(1) (*10 h)	4.224(2)	4.215(3) (*10 h)	4.196(3)	Pm-3 m/ 4.187(1) (*1600 °C/10 h)	Pm-3 m/ 4.178(1) (*10 h)	–
Crystallite size (nm)	Sint. 1700 °C/30 h	–	185	181	182	–	–	–
Theoretical density (g/cm^3)	SSR 1400 °C/6 h	BZY: 6.06 BZ: 6.21	BZ: 6.20 BZYM: 6.03	BZ: 6.22 BZYM: 5.99	BZ: 6.22 BZYM: 6.04	6.24	6.27	6.27
	Sint. 1700 °C/30 h	5,99 (*10 h)	6.03	6.02	6.07	6.13	6.13 *(10*h*)	–

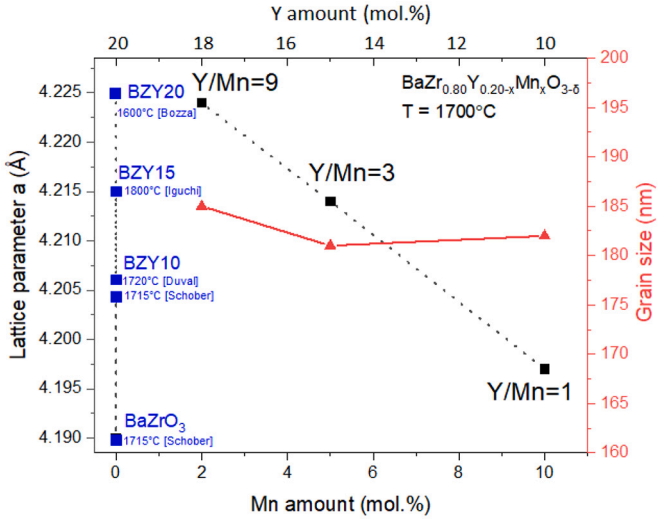

Fig. 4. Lattice parameter (black squares) and grain size (red triangles) of $BaZr_{0.8}Y_{0.2-x}Mn_xO_{3-\delta}$ (x = 0.02; 0.05; 0.1) as a function of the Y/Mn ratio in specimens sintered at 1700 °C for 30 h in air. The blue symbols point out selected literature values for pristine and Y-substituted $BaZrO_3$ [10–13]: lattice expands with Y substitution level and O deficiency δ. (For interpretation of the references to colour in this figure legend, the reader is referred to the web version of this article.)

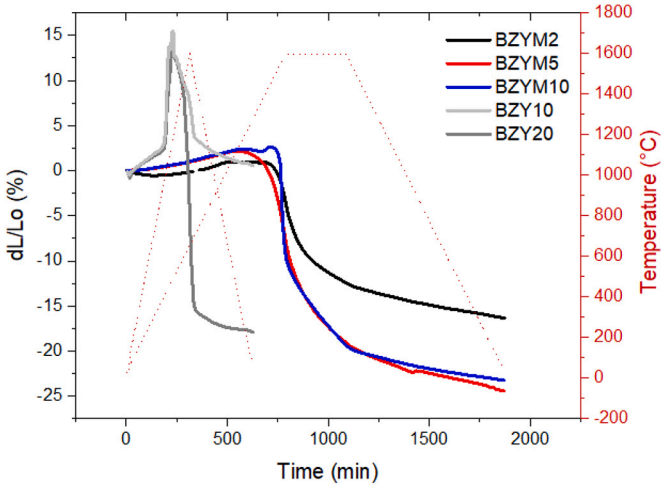

Fig. 5. Shrinkage rate dL/L_0 plotted as a function of the time and the temperature for $BaZr_{0.8}Y_{0.2-x}Mn_xO_{3-\delta}$ with x = 0.02; 0.05 and 0.1 (BZYMX). Reference compounds: $BaZr_{0.9}Y_{0.1}O_{3-\delta}$ (BZY10) and $BaZr_{0.8}Y_{0.2}O_{3-\delta}$ (BZY20).

depicted in Fig. 5, which illustrates the shrinkage rate as a function of temperature and time. For comparison, also the sintering rates of 10 and 20 mol% Y substituted $BaZrO_3$ (labelled respectively BZY10 and BZY20) are plotted. As it can be seen from the figure, samples with higher Mn content exhibit better sinterability compared to the sample with 2 mol% co-substituted Mn. This can be evidenced by the sharper drop-down of the red (BZYM5) and the blue (BZYM10) curves compared to the black one (BZYM2), and the overall larger negative (dL/L_0) values reached by first two specimens already at the beginning of the isothermal regime at $T = 1600$ °C. There is practically no difference observed in the shrinkage rates of the specimens containing 5 and 10 mol% Mn. The sintering process has not been completely finalized under the test conditions, as suggested by the curve ever descending to larger negative (dL/L_0) values in the isothermal regime. In a case of complete densification, a plateau will be reached in this graph-region.

Transition metals have been added to ceramic materials as a sintering aid because of their lower melting point than those of lanthanide [14]. As expected, the sintering behavior of BZYM2 reveals pronounced similarities to the BZY20 material. Generally, substituting Zr with more Y (10 vs 20 mol%) boosts the densification of material microstructure. Adding 2 mol% Mn to the stoichiometry in that case could be considered as undertaking sintering aid assisted approach. However, effectively there is no improvement in the sintering caused by the 2 mol% Mn "sintering aid" compared to the pristine BZY20.

Inspection of the specimen's surface after sintering revealed a different colour: in fact, the side in contact with the Pt setter plate has almost a black colour, while the one in contact with the furnace atmosphere has a greenish one. During the sintering of BZYM ceramics in ambient air, $BaCO_3$ might be formed on the surface, which after decomposition and Ba evaporation will accelerate the Y_2O_3 segregation effects. Indeed, as depicted in Fig. 6, there is a difference in the XRD patterns of the two sides of tested sample BZYM5. The side in contact with the setter plate (black pattern in Fig. 6a) reveals single phase composition, while the other side (red pattern in Fig. 6a) clearly shows Y_2O_3 segregation (Fig. 6a). There is also a shift in the peaks recorded for the two sides of the pellet, indicating for the red graph that less Y_2O_3 is present in the material due to the direct exposure to the high sintering temperatures, resulting respectively in larger Ba loss from that specimen's surface. However, the reason might be a complex of i) Ba evaporation on one side, which enhances the Y replacement from B- to A- site in the perovskite(however, Y being located on A-site in the perovskite is not matching well geometrically and thermodynamically, hence being segregated at the oxygen rich site forming Y_2O_3); and ii) Oxygen saturation at the air- exposed side of the sample, which leads to acceptor dopant segregation at the surface as compensation for the cancelled oxygen vacancies. The SEM image taken from the cross section of such a pellet reveals Y_2O_3 segregations visible as grains in darker contrast at about 5 μm distance from the surface (Fig. 6b).

3.4. Microstructure

Fig. 7 presents the microstructures of the sintered materials as a function of the Y/Mn content taken from the unpolished surface and cross sections (Fig. 7a). As observed from the surface micrographs, all of the samples sintered at 1600 °C show significant surface porosity with larger islands of a secondary phase rich to Y_2O_3. Such Y_2O_3 enriched grains cannot be observed in the cross section images, indicating that it is a surface related effect. Moreover, the bulk remains single phase and achieves almost full densification with increased Mn amount. As depicted in the microscopic images in Fig. 7b, BYZM5 sample sintered at 1700 °C reveals very dense microstructure. The relative density determined via the Archimedes method was 99.9%. Material displays grain size distribution between 0.5 to about 5 μm. It is known from the literature that Mn is a very good choice as a sintering aid for pure $BaZrO_3$ ceramics, which reaches grain size of more than 10 μm.

3.5. Coefficient of thermal expansion (α)

The thermal expansion of sintered BZYM specimens was measured in air during heating from room temperature to 1400 °C and back in cooling mode. Linear thermal expansion coefficient, α, was then calculated from Eq. 5, where L_0 and dL are respectively the initial length and the length change of the sample, while T_0 and T are the starting and the final temperature, respectively.

$$\alpha = \frac{dL}{L_0}(T - T_0) \tag{5}$$

The α for materials with different Y:Mn ratios were plotted versus the temperature (200–1400 °C) in Fig. 8a (red, indicated with *h*: heating; blue, indicated with *c*: cooling), while the corresponding dilatometric curves are presented in section *Supporting Information*, Fig. S3. The α values in heating mode lay well within the range of 7.5–10.5 $\times 10^{-6}$ K^{-1} in the measured temperature range. As references, the α of pristine $BaZrO_3$ is 7 $\times 10^{-6}$ K^{-1} [15], and α of $Ba_{1.005}Zr_{0.625}Ce_{0.2}Y_{0.175}O_{3-\delta}$ (BZCY) and of NiO:BZCY composite are depicted in Fig. 8b. The general tendency is that material expands less with decreasing the Y:Mn ratio. Correlating this observation with the lattice parameter for BZYM2, BZYM5 and BZYM10 (Table 1) shows trend consistency. BZYM2 expands the most compared to BZYM5 and BZYM10. On the other hand, following the mentioned trend, α of BZYM10 should be somewhat lower than that of the BZYM5. However, as it is seen from the figure, α of the material with 10 mol% Mn lays slightly higher above that of BZYM5 over the complete temperature range. This out-of-trend behavior might be explained by different specimens microstructure (grain size), which is indeed a common effect in polycrystalline materials [16], but also with a secondary phase, evolving during the high thermal treatment, e.g. BaO which was found to be present in some BZYM5 specimens after heat treatment. BaO is known as an additive for glasses, decreasing their thermal expansion. Finally, certain chemical expansion contributions

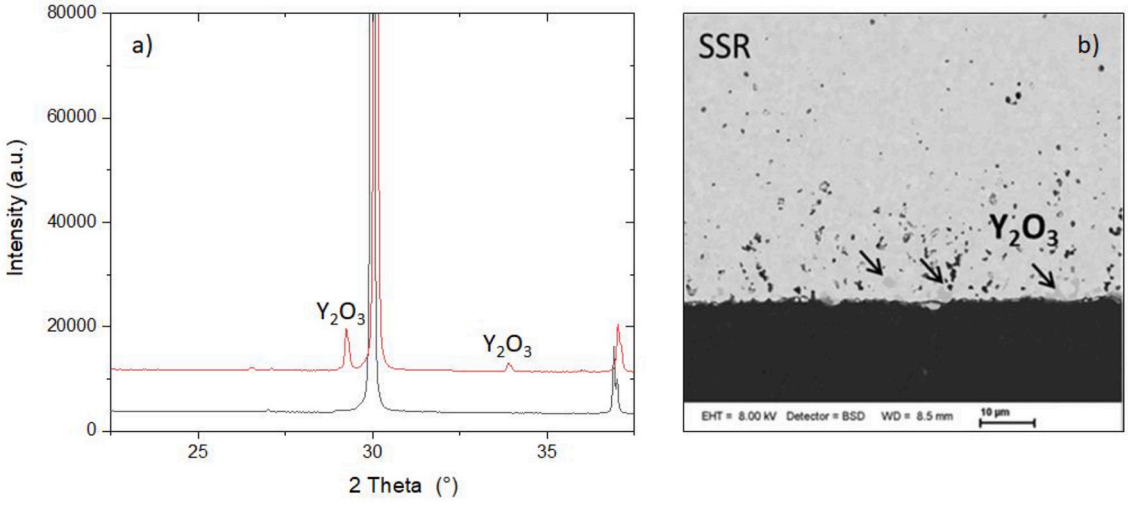

Fig. 6. a) XRD patterns of the two sides of a sintered BZYM5 sample (focused in the 20–40° region): Y_2O_3 segregated on the pellet surface, exposed to the furnace atmosphere (red pattern), while the other side remains free of such impurities (black pattern); b) SEM image of sintered BZYM5 pellet cross section showing a clearly dark-contrast between the main phase (light grey) and Y_2O_3 grains (dark grey). (For interpretation of the references to colour in this figure legend, the reader is referred to the web version of this article.)

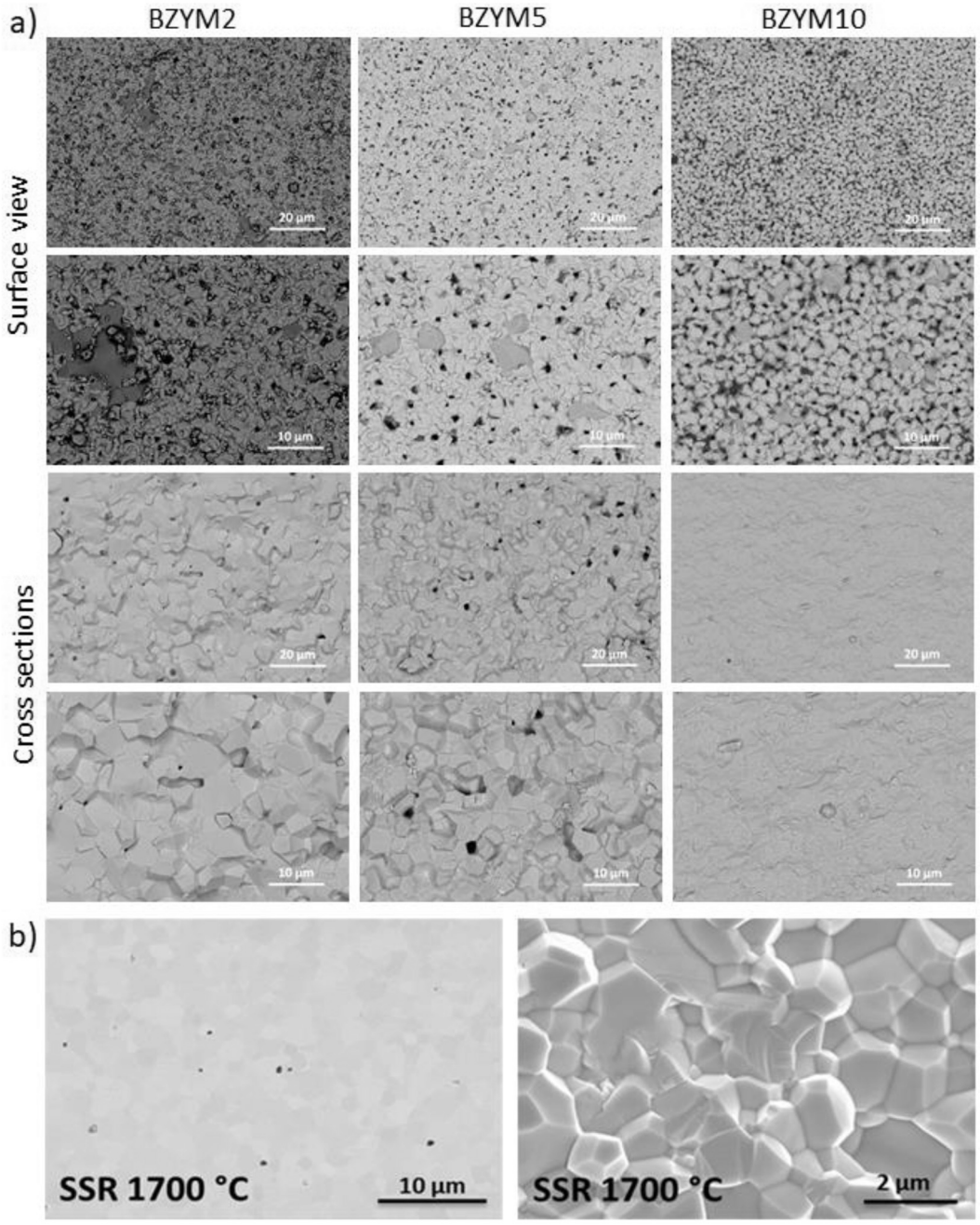

Fig. 7. Microstructure of compounds in the series $BaZr_{0.8}Y_{0.2-x}Mn_xO_{3-\delta}$. a) SEM secondary electron images from the unpolished surface and unpolished cross sections of BZYMX specimens sintered at 1600 °C for 10 h; b) SEM images from the polished surface and unpolished cross sections of BZYM5 specimen sintered at 1700 °C for 30 h.

may also be evidenced from the data plotted in Fig. 8a and Fig. S3, however these will be mostly related to stoichiometric expansion processes, rather than due to phase change (Fig. S3, no abrupt changes in the direction of the curve, which could be otherwise interpreted as transformation/transition effects.).

3.6. Water uptake

The measurements have shown reproducible real physical uptake and release of water without a chemical change in the structure. The proton concentration $[OH_O^{\bullet}]$ of specimens of the series $BaZr_{0.8}Y_{0.2-x}Mn_xO_{3-\delta}$ was calculated from the mass change detected by the thermogravimetric analysis [18], according to Eq. 6:

$$\left[OH_O^{\bullet}\right] = \frac{\Delta m}{m_0}\frac{M_{BZYM}}{0.5M_{H2O}} \tag{6}$$

Fig. 9 shows the composition dependence of the proton content. As it can be observed from the figure, the incorporation of water increases with decreasing the Mn content (10 mol% → 2 mol%) but also with decreasing the temperature (600 °C → 300 °C, reflecting the exothermic nature of the hydration reaction). As the enthalpy of the hydration reaction tends to become more exothermic with decreasing electronegativity of the cations interacting with the lattice oxygen, i.e. with decreasing Brønsted basicity of the oxide [19], an increase in the Mn content within the BZYM series will lead to an increase of the oxide basicity (electronegativity χ of Mn is 1.5 compared to that of Y (1.2) and

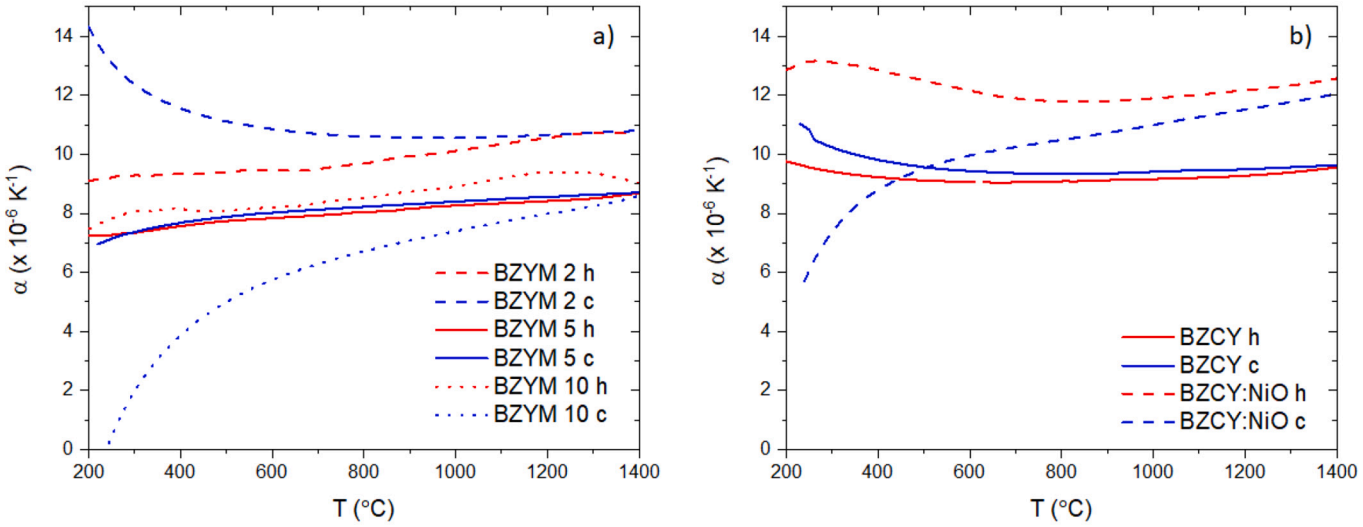

Fig. 8. CTE plotted versus the temperature for a) compounds of the series $BaZr_{0.8}Y_{0.2-x}Mn_xO_{3-\delta}$; b) BZCY and NiO:BZCY composite. Further CTE data of proton conductors and other functional materials can be found in [17].

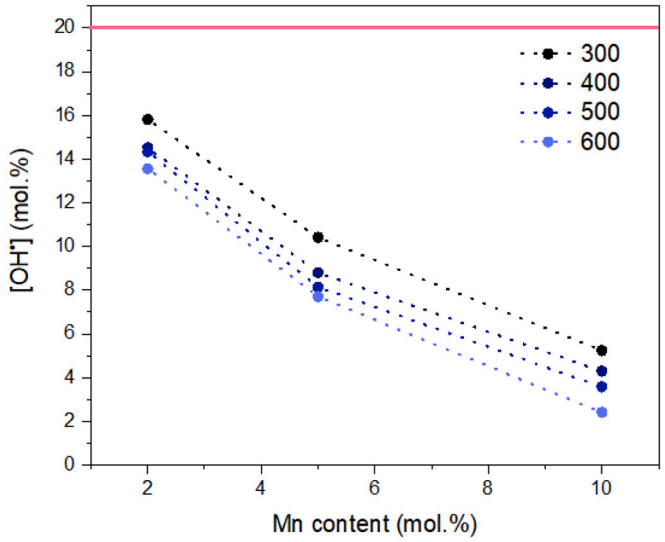

Fig. 9. Equilibrium proton concentration of $BaZr_{0.8}Y_{0.2-x}Mn_xO_{3-\delta}$ as function of the Mn content (pink lines indicate the theoretical proton content, according to the nominal stoichiometry, e.g. oxygen vacancies available to take up protons). p_{H2O} = 42.5 mbar. (For interpretation of the references to colour in this figure legend, the reader is referred to the web version of this article.)

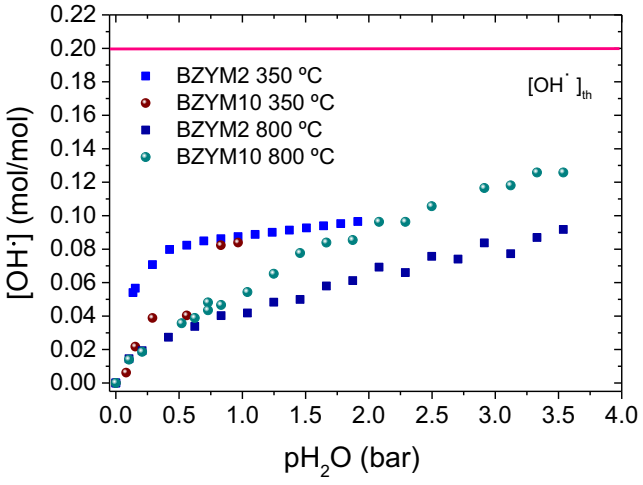

Fig. 10. a) Proton content registered for BZYM2 and BZYM10 as a function of p_{H2O} at 350 °C and 800 °C; (pink line indicates the theoretical proton content according to the nominal stoichiometry). (For interpretation of the references to colour in this figure legend, the reader is referred to the web version of this article.)

Zr (1.4)), and respectively to less favorable thermodynamics of hydration for compounds with higher Mn content. This tendency holds true and as inferred from Fig. 9: compounds with higher Y/Mn ratios are more susceptible to hydration. Since BZYM2 ($BaZr_{0.8}Y_{0.18}Mn_{0.02}O_{3-\delta}$) is compositionally analogous to the Mn-free BZY20 ($BaZr_{0.8}Y_{0.2}O_{3-\delta}$) compound, it is expected that their hydration behavior show resemblance. According to the literature data (and considering the difference in experimental procedures), BZY20 takes up to 12–15 mol% protons at 300 °C [20]. These data are generally in line with the proton uptake observed for BZYM2. The proton concentration obtained for the mixed proton-electronic conductor BZYM10 lines up well with data for other mixed conducting ceramics: for reference the summary in [21], according to which the typical range of proton uptake for such MPEC materials is well below 8 mol% at 250 °C.

Fig. 10 depicts the proton concentration (in mol/mol) for BZYM2 and BZYM10 plotted as a function of the p_{H2O} at 350 °C and 800 °C (Fig. 10a). With p_{H2O} increase, the two materials show an increase in the proton uptake, mostly pronounced for BZYM2 at lower temperatures. At 350 °C and p_{H2O} of around 0.5 bar BZYM 2 gets fully saturated (plateau), while at this condition the hydration of BZYM10 is quite negligible. The saturation tendency reported in [22] was far below the one obtained in the present work, however the maximum of proton content was not reached in any case. These observations are in accordance with Fig. 9. The fact that the proton uptake, registered for BZYM2 at these conditions, is higher than that for the BZYM10 material, can be correlated with the larger number of vacancies, available to uptake these protons, for material with higher Y:Mn ratio. This observation is in line with the composition dependence shown in Fig. 9.

3.7. Electrical conductivity

The total, bulk and grain boundary conductivities are plotted in Fig. 11 as a function of the temperature measured in 2 vol% H_2 in Ar, in humid conditions (2.5 vol% H_2O). As it can be seen from the plots, a

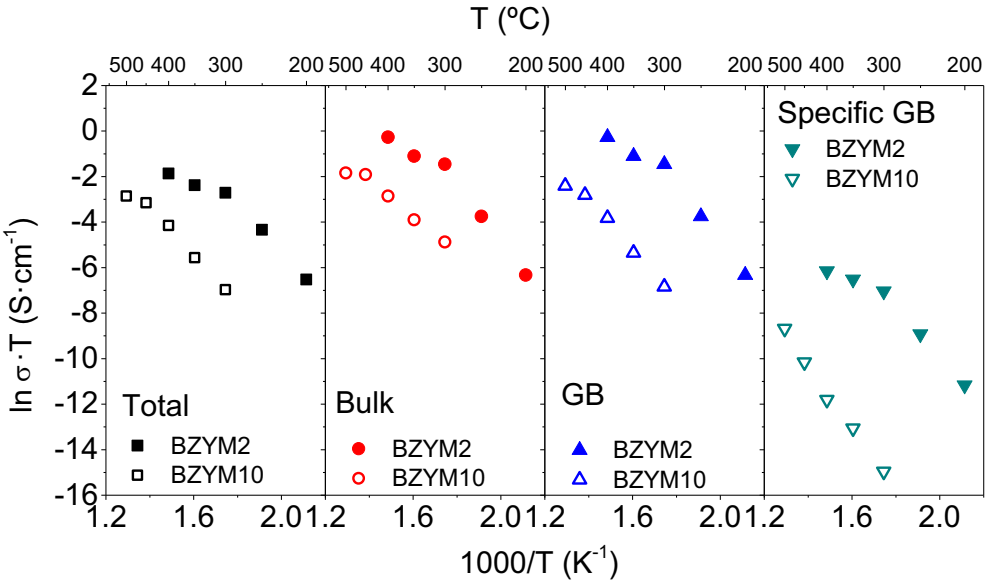

Fig. 11. EIS deconvoluted conductivity in humid (2.5 vol% H_2O), 2 vol% H_2/Ar of materials from the $BaZr_{0.8}Y_{0.2-x}Mn_xO_{3-\delta}$ series, a) total, b) bulk, c) grain boundary (GB) and d) specific grain boundary, plotted as a function of the inverse temperature.

Table 2
Bulk and grain boundary conductivity parameters deconvoluted from IES measurements on materials from the $BaZr_{0.8}Y_{0.2-x}Mn_xO_{3-\delta}$ series in humid (2.5 vol% H_2O), 2 vol% H_2/Ar.

Parameter	BZYM2	BZYM10
Ea bulk (eV)	0.44	0.62
Ea grain boundary (eV)	0.83	0.88
Ceq bulk (F)	$3.3{\cdot}10^{-11}$ -$1.6{\cdot}10^{-12}$	$7.1{\cdot}10^{-11}$ -$4.3{\cdot}10^{-10}$
Ceq grain boundary (F)	$4.2{\cdot}10^{-9}$ -$4.4{\cdot}10^{-9}$	$9.7{\cdot}10^{-10}$ -$1.9{\cdot}10^{-8}$
$\sigma_{TOTAL,\ 400\ ^\circ C}$ (S·cm^{-1})	$1.1{\cdot}10^{-4}$	$1.8{\cdot}10^{-5}$

higher total and bulk conductivity was found for the BZYM2 compared to the BZYM10 material, as expected from the hydration results. For the BZYM2, the bulk conductivity contribution could be measured only at 400 °C or lower temperature. For BZYM10, however, bulk and grain boundary contributions could be discerned until 500 °C, indicating that the Mn richer material exhibits higher specific grain boundary, influenced by the different electrostatic profiles at the grain interfaces [23]. Besides, the lower activation energy calculated from the Arrhenius plots of the BZYM2 compared to BZYM10 indicates that BZYM2 is predominantly a proton conductor, while BZYM10 is mainly an oxygen-ion and electron-hole conductor [24]. The equivalent capacitances for bulk and grain boundary are indicated in Table 2. Fig. S4 (*Supporting Information*) shows exemplarily the EIS spectra of BZYM2 and BZYM10 pellets at 350 °C. They were composed of three loops, corresponding to bulk, grain boundary and electrode impedance contributions.

3.8. NEXAFS surface characterization of $BaZr_{0.8}Y_{0.1}Mn_{0.1}O_{3-\delta}$ (BZYM10)

NEXAFS is a powerful tool to investigate local structure and valence state of atoms and it was used in the investigation of the BZYM material to probe the surrounding symmetry and oxidation state by recording spectra in the vicinity of O K-edge and Mn $L_{2,3}$-edges and comparing them with the known Mn reference oxides. Two different modes were employed: the total electron yield (TEY) mode (surface sensitive: ~10 nm) and the fluorescence yield (FY) mode (bulk-sensitive: ~100 nm).

The obtained spectra are presented in Fig. 12. The spectra of the reference Mn_2O_3 and MnO_2 powders at O K-edge (Fig. 12, top-left) are in good agreement with literature [25,26], proving the reliability and reproducibility of the experimental method. Comparison of the MnO O K-edge spectra (TEY and FY modes) shows surface oxidation of the compound with Mn_2O_3 formation at the surface: such oxidation is typical for MnO [25]. Nevertheless, the bulk of the sample corresponds to the expected MnO content. The Mn L-edge spectra of the reference powders (Fig. 12, top-right) also show good agreement with literature (for MnO, also some surface oxidation traces are noticeable) [25,26].

Fig. 12 (bottom) presents the measured spectra of the BZYM10 samples. It is important to notice that the FY spectrum at O K-edge for the pristine sample is absent due to a fluorescence detector failure. This fact is not critical for the following analysis as the main focus lies on the comparison of the oxidized and reduced BZYM10 samples and, in particular, on the analysis of the Mn L-edges that provide more localized and precise information about the Mn atoms state. Besides, the pristine state is an intermediate state between reduced and oxidized states, and can be assumed closer to the oxidized one, especially in the bulk. As for the Mn K-edge no relevant differences are observed between oxidized and pristine (cf. Fig. 12 bottom left), we can assume that the O K-edge does not behave differently, and that the discussion for the oxidized state can be valid for the pristine as well. The O K-edge spectra of the BZYM10 samples (Fig. 12, bottom-left) have the same edge position and a similar pre-edge feature. A closer look at the spectra and comparison of them to the reference spectra reveal that the main spectra shape and their onset position are similar to those of the FY (bulk) MnO spectrum. This implies that O atoms in the samples have a local symmetry close to that of MnO (rock-salt: edge-shared octahedra) [25]. Noteworthy, there are some differences in the surface region of the samples: the TEY spectra have a large intensity surge within the 535–540 eV region (especially for the pristine and reduced samples). The difference can be induced by surface carbon contamination or/and strong distortion of the octahedra.

Fig. 13 (left) shows comparison of the FY (bulk) O K-edge spectra of the oxidized and reduced BZYM10. The figure also shows the O K-edge spectra of MnO and MnO_2 powders. Although the main structure of the BZYM10 reduced and BZYM10 oxidized spectra is very similar to the MnO spectrum, the pre-edge peak (*a*) and the shoulder (*b*) reflect the presence of an additional local symmetry (rutile: distorted edge-shared octahedra) [25] of O sites that is similar to that of MnO_2. Moreover, this admixture is more prominent in the oxidized sample than in the reduced one: the *a* feature has lower intensity in the reduced BZYM10 spectrum. This fact can be crucial for the understanding of differences between the reduced and the oxidized samples. Taking into account that

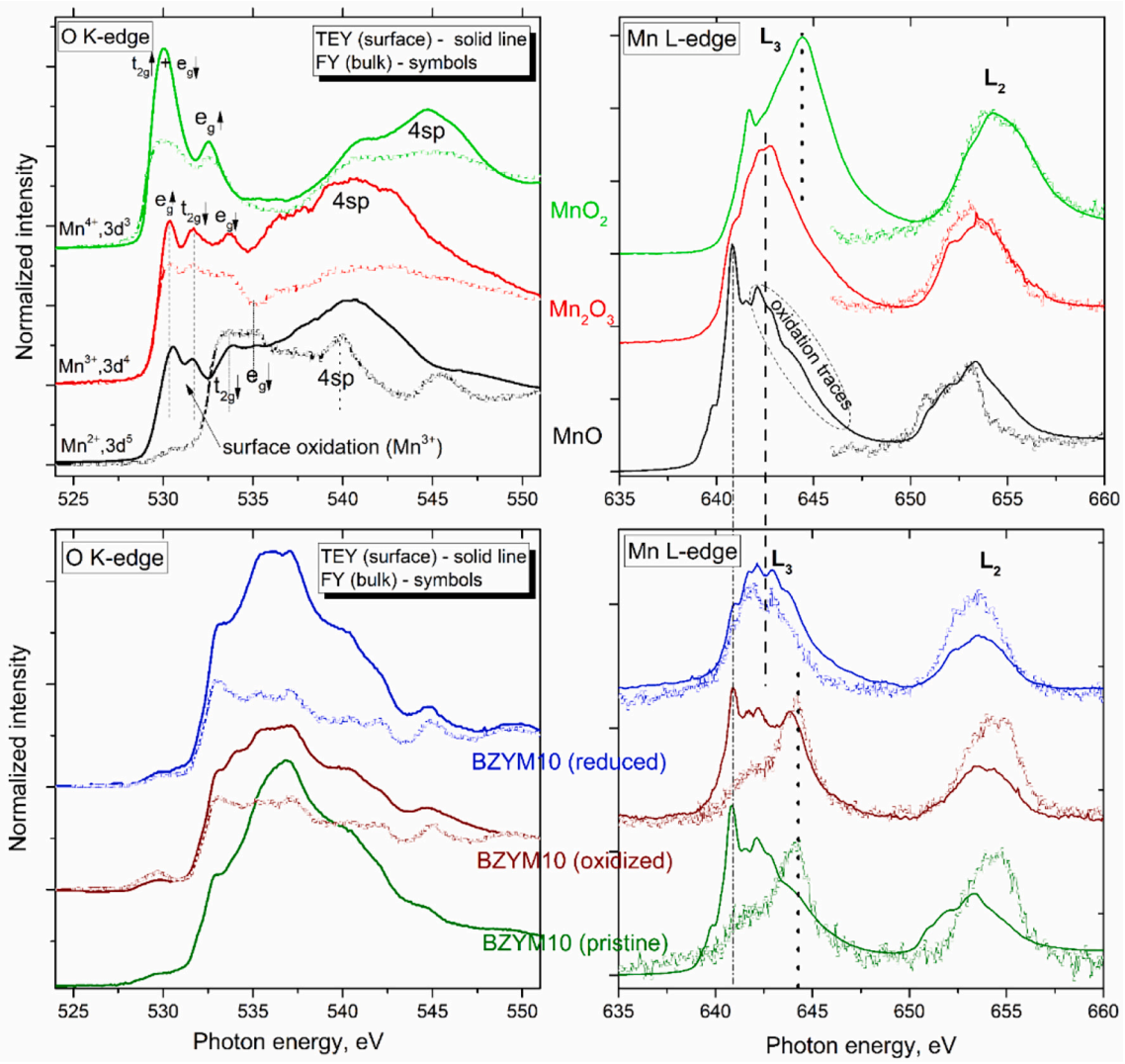

Fig. 12. Experimental NEXAFS spectra of the reference Mn oxide powders (top): MnO, Mn_2O_3, MnO_2, and the studied samples (bottom): BZYM10 pristine, BZYM10 oxidized, BZYM10 reduced. The spectra in solid line were recorded in the total electron yield (TEY) mode (surface-sensitive). The spectra acquired in the fluorescence yield (FY) mode (bulk-sensitive) are presented in symbols.

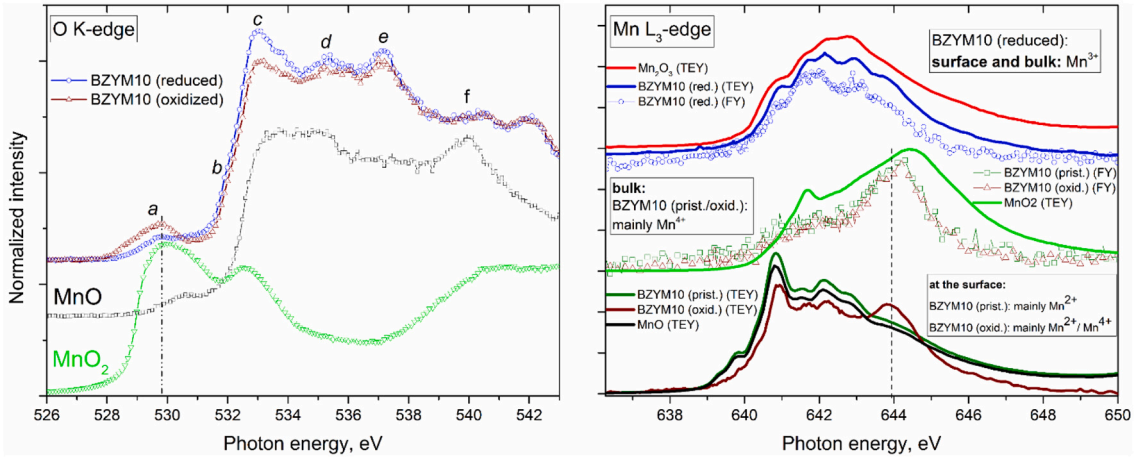

Fig. 13. Comparison of the NEXAFS spectra at O K-edge (left) and Mn L_3-edge (right) of the studied compounds and some reference powders recorded in the TEY (solid line) and FY (symbols) modes.

the *a* and *b* features corresponds to the t_{2g} and e_g states in MnO_2 (Mn 3d-O2p molecular orbitals) [26], one can assume that the reduction process is implemented through filling of the empty t_{2g} and e_g electron states in those Mn-O octahedra that are configured (connected) as in the MnO_2-like structure. Considering the Mn L-edge spectra of the BZYM10 samples (Fig. 13, right), one can notice significant difference in the signal coming from the surface and the bulk of the oxidized and pristine BZYM10. Fig. 13 (right) contains the superimposed Mn-L spectra of the BZYM10 samples and the reference powders. Based on the comparison, some important conclusions on the Mn atoms oxidation state can be made: *i)* the reduced BZYM10 sample contains Mn atoms in Mn^{3+} state both in the bulk and at the surface; *ii)* the pristine BZYM10 mainly has Mn^{4+} in the bulk and Mn^{2+} at the surface (this conclusion is in agreement with the XPS analysis of the pristine specimen, Fig. S5 section *Supporting Information*); *iii)* the oxidized BZYM10 also has Mn^{4+} in the bulk and Mn^{2+}/Mn^{4+} mixture at the surface. It is being suggested in the literature about LSM studied by NEXAFS [27], hydration was mediated by Mn oxidation and subsequent proton attachment to oxygen neighbors in exchange for oxygen-hole carriers. Based on the NEXAFS results, a similar effect could be expected for the BZYM system, although further exploration of dry versus hydrated states is needed to clarify the O-Mn redox interplay with proton incorporation at intermediate temperatures. In such a case, NEXAFS gained local structural and electron features combined with hydration and electrical behavior may serve as a guideline to design MPEC electrodes.

3.9. Application prospective of materials from the $BaZr_{0.8}Y_{0.2-x}Mn_xO_{3-\delta}$ series

3.9.1. Thermo-chemical stability in simulated WGSMR operation conditions

Mixed proton-electronic conductors find use as H_2 separation membranes in H_2 extractors and catalytic membrane reactors [28,29]. Examples are H_2 extractors and purificators, in which H_2 is separated from gas mixtures at elevated temperatures, or coal gasification process, in which water gas shift (WGS) reaction takes place in a catalytic membrane reactor utilizing a ceramic membrane for enhanced process efficiency. Such reactors and extractors operate, however, under harsh conditions, not only in terms of temperature (usually above 600 °C), but also in terms of the gas environments, usually containing steam, H_2, CO, CO_2, H_2S, ashes, etc. To be utilized in such an application niche, ceramic materials with promising levels of mixed proton-electronic conductivity need to be specifically tested in terms of their thermo-chemical stability under harsh operating conditions. Only materials with a good electrical performance and superior stability might be attractive candidates as membranes for H_2 extractors and catalytic membrane reactors. In Fig. 14, XRD patterns of BZYM5 powder specimens exposed to simulated *Syngas* and *Retentate* WGSMR conditions at temperatures from 600 °C to 900 °C are depicted. The stability of the material against the formation of carbonates depends on the temperature. BZYM5 is stable at the highest temperature and shows increasing formation of $BaCO_3$ from 800 down to 600 °C. However, the amount of carbonate formed is very low for all temperatures and lower than that found in cerium containing perovskites exposed under identical conditions in our previous investigation [6]. Moreover, a corresponding zirconia phase, which should form if the perovskite decomposes during reaction with CO_2 (Eq. 7), could not be identified, proving the relatively high thermo-chemical stability of the perovskite phase. Further investigations are needed to find out if the reaction with CO_2 "only" causes Ba depletion of the perovskite phase to a certain level or if the reaction goes to completion over time.

$$BaZr_{0.8}Y_{0.2-x}Mn_xO_{3-\delta} + CO_2 \rightarrow BaCO_3 + Zr_{0.8}Y_{0.2-x}Mn_xO_{2-\delta} \quad (7)$$

3.9.2. Thermo-chemical compatibility with other ceramic materials

BZYMn material itself, even though showing triple conduction, does not exhibit electronic conductivity levels sufficient to be used as electrode material without addition of a high electronic conductor, i.e. forming a cer-cer composite or a cermet. However, it can bring the advantage of avoiding full blocking of the electrons in the primary ionic phase, thus extending the electrode reacting region beyond the triple phase but across the bulk. From application point of view, materials from the $BaZr_{0.8}Y_{0.2-x}Mn_xO_{3-\delta}$ series of the present study, might have potential in cell electrode design, especially using compounds with larger Mn content, e.g. BZYM10, or dual-phase materials (cer-cer composite [30,31]), developed on their basis, e.g. BZYM10:LSM. Therefore, it is important to examine the compatibility of promising mixed proton-electronic conductors with established proton conducting electrolytes, but also with another ceramic electron conductors, used potentially as a second phase of the cer-cer electrode composite. For the purposes of cathode screening for Proton Ceramic Cells, it might be appealing investigating a composite based on BZYM10 (single phase material with most Mn along the series studied) and LSM.

In the present compatibility study, BZCY721 material was selected as a state-of-the-art ceramic proton conductor, serving as a solid electrolyte for the development of various electrochemical devices. LSM was

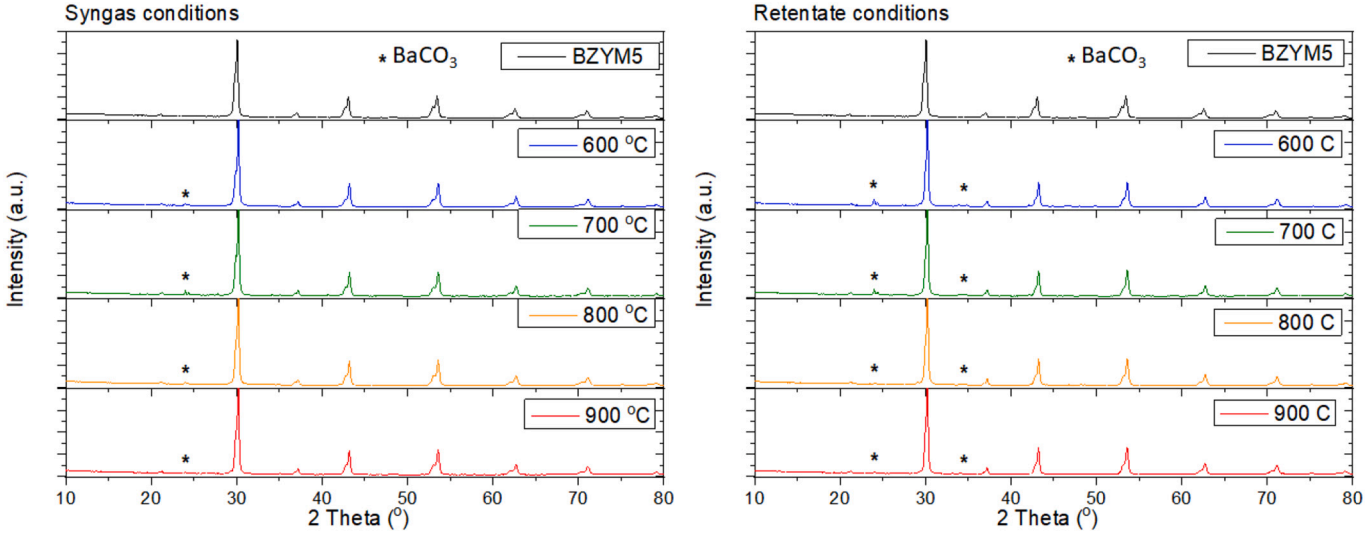

Fig. 14. XRD patterns of BZYM5 powder specimens, before (black pattern) and after exposure to simulated *Syngas* and *Retentate* WGSMR conditions at temperatures from 600 °C to 900 °C.

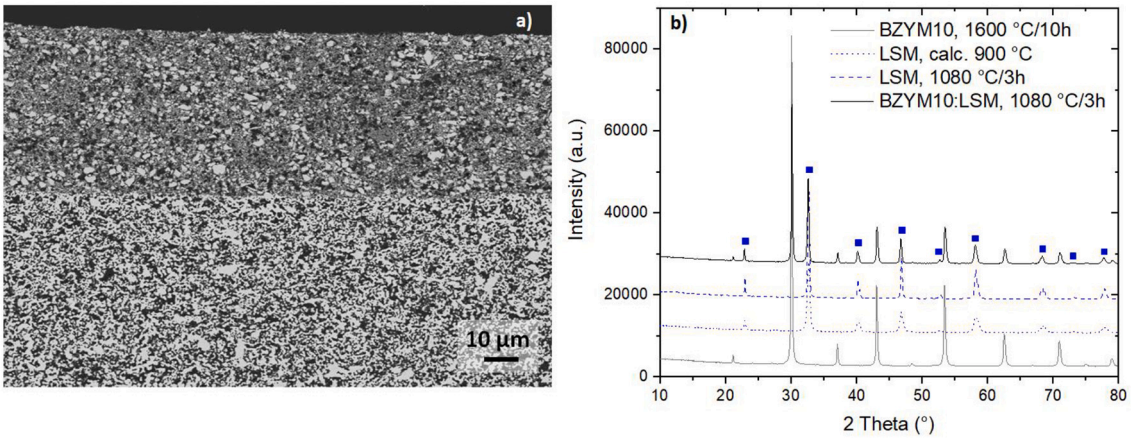

Fig. 15. a) SEM image in BSE mode: polished cross section of BZCY721 pellet ($Ba_{1.01}Zr_{0.7}Ce_{0.2}Y_{0.1}O_{3-\delta}$, $T_{sint.}$ = 1600 °C, 10 h) with a BZYM10 top layer after heat treatment at 1080 °C/3 h; b) XRD patterns of *i)* pristine BZYM10 (grey bottom); *ii)* pristine LSM after calcination at 900 °C (blue dotted); *iii)* pristine LSM after final treatment at 1080 °C/3 h (blue dashed); *iv)* cer-cer composite BZYM10:LSM after heat treatment at 1080 °C/3 h (black top). (For interpretation of the references to colour in this figure legend, the reader is referred to the web version of this article.)

selected as a state-of-the-art electronic conductor in SOFC electrode design.

Fig. 15 presents results of the compatibility tests. SEM image of BZCY721| BZYM10 polished cross section after heat treatment at conditions typical for electrode sintering (1080 °C/3 h) is shown in Fig. 15a. As it is seen from the figure, backscattered electron imaging mode reveals clean interface between the two ceramic materials without indications for intermediate phase formation. A visual inspection of the assembly after heat treatment did not reveal any delamination issues, which otherwise originate from possible thermal mismatches between the two materials. Fig. 15b shows XRD pattern of the BZYM10:LSM powder mixture as heat treated at 1080 °C for 3 h. Additionally, reference patterns for pristine BZYM10 and LSM powders were added. The fact that besides the two main phases in the BZYM10:LSM cer-cer composite, no other compounds were formed as side phases at the given processing conditions, is a clear indication for the good compatibility between these two materials.

4. Conclusions

A thorough characterization of Y and Mn co-substituted $BaZrO_3$ has been performed in order to assess the suitability of these materials for use in solid state proton electrochemical cells. The addition of Mn to the $BaZr_{0.8}Y_{0.2-x}Mn_xO_{3-\delta}$ structure (by substituting Yttrium) forms a single cubic phase of Pm-3 m symmetry up to 10 mol% of Mn. The crystal lattice constant decreases with increasing the Mn amount although the complete incorporation of substituents in the host lattice does not occur until the highest temperatures are reached (ca. 1700 °C). Mn plays a role as a sintering aid, especially above 5 mol% of substitution in the perovskite lattice. The study of the final samples composition by ICP-OES has shown they suffer from barium evaporation due to the high sintering temperature required to obtain dense specimens. Ba deficiency can be compensated by the addition of 3.5 wt% excess of $BaCO_3$ to the pristine mixture of oxides. At the surface of dense specimens, however, the inhomogeneities due to Barium loss and Y_2O_3 rich islands can be eliminated by grinding the surface of the pellet, since they only affect the most external layers of the sample. SEM micrographs confirm that the bulk remains single phase and achieves almost full densification with increased Mn amount. Coefficient of thermal expansion values in heating mode lay well within the range of $7.5–10.5{\cdot}10^{-6}\,K^{-1}$ in the measured temperature range, being higher for those with lower Mn amount.

Water uptake and hydration at constant temperature showed an improved reaction with the water for the samples with less amount of Manganese. Thus, a better hydration behavior, respectively proton conductivity, is expected for materials with closer composition to BZY (as BZYM2). The hydration behavior is in agreement with the conductivity performance at low temperature, which shows higher conductivity and lower activation energy for BZYM2, as corresponds with a better protonic conductor, while BZYM10 behaves as an oxygen and electronic mixed conductor.

Surface analysis by XPS and NEXAFS disclosed that the majority of surface Mn in BZYM10 is present as Mn^{2+}, while different oxidation states contributing to the electronic transport are ascertained in the bulk.

Finally, stability of BZYM5 in WGSMR conditions (*Syngas:* 34 vol% CO; 51 vol% H_2O; 15 vol% H_2 and *Retentate:* 90 vol% CO_2; 9.9 vol% H_2O; 0.1 vol% H_2 atmospheres) and compatibility of BZYM10 with state of the art materials for electrodes and electrolytes has been assessed. Although Mn substituted BZY materials are compatible with other cell components, exposure to acid gases as CO, CO_2 provokes the barium to form carbonates, eventually preventing the use of these bare materials in reactions involving carbon containing gases. Stabilization strategies as protective layers or design of composites could be considered to improve the performance of BZYMx materials. For the purposes of cathode screening for Proton Ceramic Cells, it might be appealing investigating a composite based on BZYM10 (single phase material with most Mn along the series studied) and LSM: the two materials are quite compatible at the temperatures of cathode sintering, as we show in the study, and next electrochemical tests might judge this strategy as possibly productive.

Declaration of Competing Interest

There are no conflicts to declare.

Acknowledgements

The authors would like to thank the Helmholtz Association of German Research Centres, Germany, under the MTET Program. Furthermore, we acknowledge Dr. V. Nischwitz and Dr. A. Besmehn from ZEA-3 at Forschungszentrum Jülich GmbH for carrying out the ICP-OES and the XPS analyses, Mrs. Eng. M.-T. Gerhards (IEK-1) for the TG measurements, Dr. C. Dellen (IEK-1) for the SEM imaging and Dr. R. Merkle from Max Planck Institute for Solid State Research (MPI-FKF) in Stuttgart, Germany for her supporting in specimens' preparation used in the NEXAFS section. We acknowledge the Helmholtz-Zentrum Berlin for provision of beam time at BESSYII, and we would like to thank the beamline scientists A. Makarova and D. Smirnov for assistance during the experiments and the useful discussions.

Appendix A. Supplementary data

Supplementary data to this article can be found online at https://doi.org/10.1016/j.ssi.2022.115959.

References

[1] S. Escolastico, M.E. Ivanova, C. Solis, S. Roitsch, W.A. Meulenberg, J.M. Serra, RSC Adv. 2 (11) (2012) 4932, https://doi.org/10.1039/c2ra20214j.
[2] F.A. Kröger, The Chemistry of Imperfect Crystals, North-Holland Pub. Co.; Interscience Publishers, Amsterdam, New York, 1964.
[3] F.W. Poulsen, Solid State Ionics 129 (1–4) (2000) 145, https://doi.org/10.1016/S0167-2738(99)00322-7.
[4] S.M. Haile, G. Staneff, K.H. Ryu, J. Mater. Sci. 36 (5) (2001) 1149, https://doi.org/10.1023/A:1004877708871.
[5] N. Bonanos, B.C.H. Steele, E.P. Butler, Impedance Spectroscopy: Theory, Experiment, and Applications, 2nd edition, 2005, p. 205, https://doi.org/10.1002/0471716243.ch4.
[6] D. van Holt, E. Forster, M.E. Ivanova, W.A. Meulenberg, M. Muller, S. Baumann, R. Vassen, J. Eur. Ceram. Soc. 34 (10) (2014) 2381, https://doi.org/10.1016/j.jeurceramsoc.2014.03.001.
[7] E. Forster, D. van Holt, M.E. Ivanova, S. Baumann, W.A. Meulenberg, M. Muller, J. Eur. Ceram. Soc. 36 (14) (2016) 3457, https://doi.org/10.1016/j.jeurceramsoc.2016.05.021.
[8] P.G. Sundell, M.E. Bjorketun, G. Wahnstrom, Phys. Rev. B 73 (2006) 10, https://doi.org/10.1103/PhysRevB.73.104112.
[9] W. Deibert, M.E. Ivanova, Y.Y. Huang, R. Merkle, J. Maier, W.A. Meulenberg, J. Mater. Chem. A (2021), https://doi.org/10.1039/d1ta05240c.
[10] T. Schober, H.G. Bohn, Solid State Ionics 127 (3–4) (2000) 351, https://doi.org/10.1016/S0167-2738(99)00283-0.
[11] S.B.C. Duval, P. Holtappels, U.F. Vogt, U. Stimming, T. Graule, Fuel Cells 9 (5) (2009) 613, https://doi.org/10.1002/fuce.200800170.
[12] F. Iguchi, N. Sata, T. Tsurui, H. Yugami, Solid State Ionics 178 (7–10) (2007) 691, https://doi.org/10.1016/j.ssi.2007.02.019.
[13] F. Bozza, K. Bator, W.W. Kubiak, T. Graule, J. Eur. Ceram. Soc. 36 (1) (2016) 101, https://doi.org/10.1016/j.jeurceramsoc.2015.09.010.
[14] N. Nasani, Z. Shakel, F.J.A. Loureiro, B.B. Panigrahi, B.B. Kale, D.P. Fagg, J. Alloys Compd. 862 (2021), https://doi.org/10.1016/j.jallcom.2021.158640.
[15] S. Yamanaka, M. Fujikane, T. Hamaguchi, H. Muta, T. Oyama, T. Matsuda, S. I. Kobayashi, K. Kurosaki, J. Alloys Compd. 359 (2003) 109, https://doi.org/10.1016/S0925-8388(03)00214-7.
[16] A. Løken, S. Ricote, S. Wachowski, Crystals 8 (2018) 9, https://doi.org/10.3390/cryst8090365.
[17] M.E. Ivanova, W.A. Meulenberg, J. Palisaitis, D. Sebold, C. Solis, M. Ziegner, J. M. Serra, J. Mayer, M. Hansel, O. Guillon, J. Eur. Ceram. Soc. 35 (4) (2015) 1239, https://doi.org/10.1016/j.jeurceramsoc.2014.11.009.
[18] T. Schober, J. Friedrich, Solid State Ionics 113 (1998) 369, https://doi.org/10.1016/S0167-2738(98)00302-6.
[19] K.D. Kreuer, Annu. Rev. Mater. Res. 33 (1) (2003) 333, https://doi.org/10.1146/annurev.matsci.33.022802.091825.
[20] S.B.C. Duval, Y-Substituted Barium zirconate, a Proton Conducting Electrolyte for Applications at Intermediate Temperatures, Dissertation, 2008.
[21] R. Zohourian, R. Merkle, G. Raimondi, J. Maier, Adv. Funct. Mater. 28 (2018) 35, https://doi.org/10.1016/j.ssi.2016.09.012.
[22] F. Krug, T. Schober, T. Springer, Solid State Ionics 81 (1–2) (1995) 111, https://doi.org/10.1016/0167-2738(95)00168-6.
[23] C. Kjolseth, H. Fjeld, O. Prytz, P.I. Dahl, C. Estournes, R. Haugsrud, T. Norby, Solid State Ionics 181 (5–7) (2010) 268, https://doi.org/10.1016/j.ssi.2010.01.014.
[24] S.P. Shafi, L. Bi, S. Boulfrad, E. Traversa, J. Electrochem. Soc. 162 (14) (2015) F1498, https://doi.org/10.1149/2.0701514jes.
[25] B. Gilbert, B.H. Frazer, A. Belz, P.G. Conrad, K.H. Nealson, D. Haskel, J.C. Lang, G. Srajer, G. De Stasio, J. Phys. Chem. A 107 (16) (2003) 2839, https://doi.org/10.1021/jp021493s.
[26] L. Laffont, P. Gibot, Mater. Charact. 61 (11) (2010) 1268, https://doi.org/10.1016/j.matchar.2010.09.001.
[27] N. Wang, S. Hinokuma, T. Ina, H. Toriumi, M. Katayama, Y. Inada, C.Y. Zhu, H. Habazaki, Y. Aoki, Chem. Mater. 31 (20) (2019) 8383, https://doi.org/10.1021/acs.chemmater.9b02131.
[28] W. Deibert, M.E. Ivanova, S. Baumann, O. Guillon, W.A. Meulenberg, J. Membr. Sci. 543 (2017) 79, https://doi.org/10.1016/j.memsci.2017.08.016.
[29] J. Franz, V. Scherer, Enrgy Proced 4 (2011) 645, https://doi.org/10.1016/j.egypro.2011.01.100.
[30] M.E. Ivanova, S. Escolastico, M. Balaguer, J. Palisaitis, Y.J. Sohn, W. A. Meulenberg, O. Guillon, J. Mayer, J.M. Serra, Sci. Rep.-UK 6 (2016), https://doi.org/10.1038/srep34773.
[31] E. Rebollo, C. Mortalo, S. Escolastico, S. Boldrini, S. Barison, J.M. Serra, M. Fabrizio, Energy Environ. Sci. 8 (12) (2015) 3675, https://doi.org/10.1039/c5ee01793a.